J Adv Ceram

Research Article

Exceptional mechanical properties of $(Ti_{1-x}Zr_x)_2AlC$ MAX phase coatings with amorphous-nanocrystalline oxidation layers

Kaihang Wang[1,2], Yan Zhang[1], Guanshui Ma[1], Yuxi Xu[1,2], Zhenyu Wang[1,2,✉], Aiying Wang[1,2,✉]

Cite this article: Wang K, Zhang Y, Ma G, et al. *J Adv Ceram* 2026, **15**(1): 9221201. https://doi.org/10.26599/JAC.2025.9221201

ABSTRACT: The brittleness of hard ceramic materials poses a significant challenge to their practical application because of the trade-off between hardness and toughness. Here, we propose a hierarchical structure strategy that utilizes alloying and vacuum oxidation to fabricate MAX phase coatings with an amorphous-nanocrystalline oxidation layer on the surface. Hierarchical $(Ti_{1-x}Zr_x)_2AlC$ coatings (x = 0.05–0.18) were prepared via magnetron sputtering followed by vacuum annealing, and the hardness and fracture toughness increased simultaneously with increasing Zr content. A maximum hardness of 19.4 GPa and fracture toughness of 4.1 MPa·m$^{1/2}$ were achieved in the $(Ti_{0.82}Zr_{0.18})_2AlC$ coating, significantly surpassing previously reported MAX phase coatings. The enhanced hardness primarily originated from the formation of solid solutions of Zr at the M-site and second phase Zr_3Al_2, whereas the exceptional toughness was attributed to the amorphous-nanocrystalline structure in the surface oxidation layer and the gradient structure of the coatings. These findings provide a pioneering approach based on alloying and oxidation for developing hard yet tough MAX phase coatings and other ceramic materials.

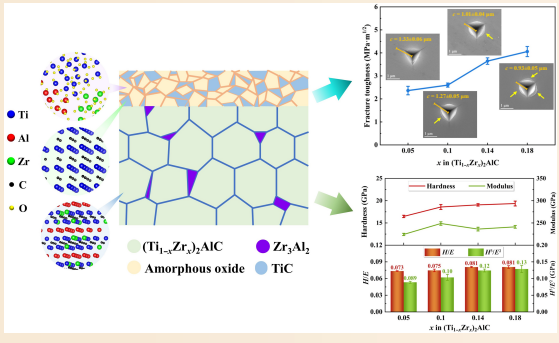

KEYWORDS: MAX phase coating; hardness–toughness; solid solution; amorphous-nanocrystalline; gradient structure

1 Introduction

The high hardness of ceramic materials endows them with remarkable wear and impact resistance, making them widely used as coatings for surface protection [1]. Nevertheless, they are inherently brittle and prone to cracking even under slight deformation. Therefore, improving the toughness of ceramic coatings has long been a major challenge in their practical application. The construction of heterogeneous nanostructures, such as nanotwinned, gradient, and dual-phase nanostructures, provides a strategy for this hardness–toughness trade-off, as it facilitates strain delocalization and suppresses the formation of a single major crack [2–5]. As a result, heterogeneous nanostructured metals exhibit significantly improved ductility and toughness when their high strength is preserved. Although this strategy was proposed for metals, multiple heterogeneous nanostructured ceramic coatings have been reported to exhibit exceptional ductility or toughness [6–8]. However, it is not easy to construct these structures for specific materials.

MAX phases represent a class of ternary layered materials characterized by alternately stacked MX building blocks and A layers, where M denotes an early transition metal element, A denotes an element from groups 13 to 16, and X can be C, N, or B [9]. A mixture of M–X covalent bonds and M–A metallic bonds endows MAX phases with an exceptional combination of ceramic and metallic properties, such as moderate toughness, machinability, remarkable oxidation and corrosion resistance, rendering them strong candidates for protective coatings in harsh environments [10]. However, compared with those in typical structural ceramics, the relatively weak M–A bonds in MAX phases compromise their hardness [11]. Although the nanocrystalline structure enhances the hardness of MAX phase coatings to 10–15 GPa, these values are still far below those of typical carbide and nitride hard coatings [12–14]. Some studies have shown good ductility and toughness in Cr_2AlC MAX phase coatings owing to the activation of multiple plastic deformation mechanisms involving nonbasal sliding and shear banding when the grain size is reduced to the nanoscale [15,16]. However, like most metals and ceramics, nanocrystalline MAX phase coatings exhibit significantly lower fracture toughness than corresponding bulk materials [17]. Therefore, enhancing the hardness and fracture toughness of MAX phase coatings via composition and structural design is crucial.

Quaternary Ti–Zr–Al–C MAX phases have recently attracted

[1] State Key Laboratory of Advanced Marine Materials, Zhejiang Key Laboratory of Extreme-environmental Material Surfaces and Interfaces, Ningbo Institute of Materials Technology and Engineering, Chinese Academy of Sciences, Ningbo 315201, China. [2] College of Materials Science and Opto-Electronic Technology, University of Chinese Academy of Sciences, Beijing 100049, China.

✉ Corresponding authors. E-mail: Z. Wang, wangzy@nimte.ac.cn; A. Wang, aywang@nimte.ac.cn

Received: August 11, 2025; Revised: October 11, 2025; Accepted: November 7, 2025

extensive interest for their promising applications in the nuclear industry [18–23]. Since Zr has a large atomic size mismatch with Ti, a solid solution of Zr at the M-site of MAX phases is expected to have high hardness [24,25]. In our previous work [26], a high-purity $(Ti_{0.9}Zr_{0.1})_2AlC$ solid solution coating was fabricated via high-power impulse magnetron sputtering (HiPIMS) deposition technology followed by a vacuum annealing process. Compared with the monolithic Ti_2AlC coating, the $(Ti_{0.9}Zr_{0.1})_2AlC$ coating presented a 30% improvement in hardness, but the fracture toughness deteriorated because of grain refinement and the formation of Zr-rich intergranular phases. Atomic-scale calculations based on density functional theory (DFT) suggest that increasing the Zr content in $(Ti_{1-x}Zr_x)_2AlC$ ($x < 0.33$) increases its hardness but has no effect on toughness [22]. The construction of heterogeneous nanostructures is expected to be a breakthrough in overcoming the hardness–toughness trade-off. Oxygen incorporation into the coating during annealing may result in a fine-grained region on the surface [27]. Moreover, owing to the utilization of HiPIMS technology and the two-step method, annealing only at an intermediate temperature for a short time can result in the formation of a $(Ti,Zr)_2AlC$ solid solution in the coatings [26]. Under these conditions, an amorphous or composite amorphous-nanocrystalline layer may also form on the surface [28]. Therefore, increasing the annealing pressure properly to promote oxidation is likely to generate heterogeneous nanostructures, thereby improving the fracture toughness.

In this work, we fabricated hierarchical $(Ti_{1-x}Zr_x)_2AlC$ coatings with various Zr contents via HiPIMS deposition and vacuum annealing. A comprehensive characterization of the phase, composition and microstructure revealed the formation of a crystalline $(Ti_{1-x}Zr_x)_2AlC$ solid solution and an amorphous-nanocrystalline oxidation layer on the surface, thereby forming a gradient structure. The mechanical properties were investigated via nanoindentation and micropillar compression tests. The results show that increasing the Zr content up to $x = 0.18$ significantly improved both the hardness and fracture toughness. The fracture behavior and deformation mechanisms were investigated in terms of microstructural evolution via transmission electron microscopy (TEM) analysis.

2 Experimental

Ti–Zr–Al–C coatings with different Zr contents were deposited on Ti–6Al–4V titanium alloy and WC–8Co carbide alloy substrates in a custom-made multitarget magnetron sputtering system using a TiAl alloy target (Ti : Al = 1 : 1 at%), a graphite target and a zirconium target. Before deposition, to eliminate surface contaminants and oxides, the substrates were etched by Ar^+ using a pulsed bias of −400 V. During deposition, Ar as the working gas was introduced into the chamber to maintain a constant pressure of 0.7 Pa. The sample holder was maintained at 200 °C. A pulsed bias of −70 V was applied to the substrates. Directly prior to depositing the Ti–Zr–Al–C coating, a 0.2–0.3 μm thick $TiAl_x$ interlayer was predeposited to enhance the adhesion between the coating and the substrate. The TiAl target was operated via HiPIMS with a duty ratio of 5%, a frequency of 1000 Hz and an average power of 150 W. The graphite target was operated via direct current magnetron sputtering (DCMS) at a power of 45 W. Different Zr contents in the coatings were achieved by altering the sputtering power of the Zr target. The Zr target was operated via HiPIMS at average powers of 15, 20, 25, and 30 W for samples S1, S2, S3, and S4, respectively, with a duty ratio of 2.5% and a frequency of 1000 Hz. The as-deposited Ti–Zr–Al–C coatings were annealed in a thermal process furnace (RTP S304, JouleYacht, China) to form crystalline MAX phases. The initial pressure in the furnace prior to heating was controlled at 2×10^{-3} Pa. A slightly high pressure favors the formation of surface nanostructures. The coatings were held at 750 °C for 90 min to form $(Ti_{1-x}Zr_x)_2AlC$. A heating rate of 30 °C/min and a cooling rate of 7.5 °C/min were used.

The phase compositions of the coatings were investigated via an X-ray diffractometer (XRD; D8 Discover, Brucker, Germany) in θ–2θ mode with Cu Kα radiation over a 2θ range of 10°–90°. The lattice parameters of the MAX phase with diverse Zr contents were determined by Rietveld refinement using the fundamental parameters method in Bruker TOPAS software. Chemical compositional depth analysis of the coatings was performed via a glow discharge optical emission spectrometer (GDOES; GDA 750HP, Spectruma, Germany). The sample surface was etched by Ar^+ in a 3 mm diameter area to a depth of approximately 6 μm beyond the entire coating thickness to obtain composition depth profiles of the coatings. The surface chemical components were measured by an X-ray photoelectron spectroscope (XPS; AXIS SUPRA, Kratos, UK) using monochromatic Al Kα radiation (1486.6 eV). All the XPS peaks were calibrated to the C 1s adventitious peak at 284.8 eV. The sample morphologies were investigated via a thermal field emission scanning electron microscope (SEM; Quanta FEG 250, FEI, USA). The microstructure observation was accomplished by TEM (Talos F200X, Thermo Fisher, USA). In particular, the atom-scale characterization was performed via a CS-corrected TEM (Scientific Spectra 300, Thermo Fisher, USA). The cross-sectional TEM sample was prepared by focused ion beam (FIB; Thermo Fisher Helios G4 CX).

The plane residual stress (σ_r) of the coatings was measured via a two-dimensional X-ray diffractometer (D8 Discover, Brucker, Germany) using the $\sin^2\psi$ method. It was calculated as Eq. (1):

$$\sigma_r = -\frac{E}{2(1+\nu)}\cot\theta\frac{\partial 2\theta}{\partial \sin^2\psi} \quad (1)$$

where E is the elastic modulus measured by nanoindentation, ν is Poisson's ratio (0.19, taken from Ti_2AlC), θ is the Bragg angle, and ψ is the off-axis angle with respect to the sample surface normal. Because the relative magnitudes of the σ_r in the four coatings are of concern, it is reasonable to use the isotropic E measured by nanoindentation. The diffraction peak near 60° corresponding to the (110) reflection was selected for the stress calculation because it had a high intensity and did not overlap with the other peaks. ψ ranged from 0 to 60°. The average of two components along the length and width directions of the substrates was calculated as the residual stress of the coatings [29].

The hardness (H) and elastic modulus (E) of the coatings were measured via a nanoindenter (G200, MTS, USA) equipped with a Berkovich diamond tip in continuous stiffness measurement (CSM) mode. The maximum pressed depth was set to approximately 600 nm. To limit the influence of the substrate, the values of H and E were determined at a depth of 350 nm, which is approximately 10% of the coating thickness. Each sample was measured eight times to minimize errors.

The fracture toughness of the coatings was evaluated via the same nanoindenter, but with a cube-corner diamond tip in load-controlled mode. This sharper indenter can generate cracks at a smaller load, thereby reducing the substrate effect. The fracture toughness can be calculated from the length of the radial cracks and the load. For stress-free materials, the fracture toughness is equal to the critical stress intensity factor (K_{IC}) (Eq. (2)) [30]:

$$K_{IC} = \alpha\left(\frac{E}{H}\right)^{1/2}\frac{P}{c^{3/2}} \quad (2)$$

where P is the load, c is the total length of the radial crack from the indentation center to the crack tip determined from SEM images, and α is an empirical parameter dependent on the centerline-to-face angle (ψ) of the indenter (35.3° for the cube-corner indenter) and Poisson's ratio (ν) given by Eq. (3) [30]:

$$\alpha = \frac{0.0352}{1-\nu}(\cot\psi)^{1/3} \quad (3)$$

Considering the existence of residual compressive stress in the coatings, the actual fracture toughness (K_C) was estimated as Eq. (4) [31]:

$$K_C = K_{IC} + Z\sigma_r c^{1/2} \quad (4)$$

where Z is the crack geometry factor. For typical radial cracks, Z is 0.61 [31]. A load of 50 mN was used to analyze the microstructure evolution of the indentation cross-section by TEM.

The uniaxial mechanical properties were determined via micropillar compression tests using a PI85 PicoIndenter (Hysitron, USA) in SEM. The micropillars were milled by FIB into cylinders of approximately Φ1.2 μm × 2.4 μm, with an aspect ratio of 2 : 1. A tiny milling current was finally used to minimize the taper of the cylindrical micropillar and potential damage to the micropillar surface from the Ga^+ ion beam. The micropillars were compressed via a flat-ended diamond indenter with a bottom diameter of 5 μm in displacement-control mode at a squeezing velocity of 5 nm/s (corresponding strain rate of 0.0021 s^{-1}). The compression was performed until failure, which can be observed via SEM. The true stress $\sigma = (P/A_0)\times(1-\Delta h/h_0)$ and true strain $\varepsilon = \ln(1-\Delta h/h_0)$ were calculated, where P is the compressive load, A_0 is the initial cross-sectional area of the micropillar, h_0 is the initial height of the micropillar, and Δh is the indenter displacement.

3 Results and discussion

3.1 Compositions and structures

$(Ti_{1-x}Zr_x)_2AlC$ coatings were fabricated via HiPIMS deposition and vacuum annealing. XRD patterns (Fig. 1(a)) revealed the presence of a high-purity Ti_2AlC MAX phase (ICDD No. 00-029-0095) in the coatings. All major reflections showed no intensity anomalies, indicating negligible preferred orientation. However, since Zr has a larger atomic size than Ti does, Zr incorporation led to a downshift of the peaks identified as MAX phases, with the peaks gradually shifting to lower angles as the Zr content increased. Moreover, the substrate peak (α-Ti) remained at the same position regardless of the Zr content, as evidenced by the 2θ range of 59°–65° (Fig. 1(b)). Thus, this exclusive shift in the Ti_2AlC reflections confirms that lattice expansion occurred due to the gradual substitution of Zr at the M-site. Minor TiAl and Ti_3Al peaks exhibited no shift, suggesting that these phases were likely present in the substrate or interlayer. Notably, the Zr_3Al_2 phase emerged in the S3 and S4 samples without a visible TiAl phase, indicating the greater chemical affinity of Al for Zr than for Ti.

Rietveld refinement of the XRD patterns (Fig. S1 in the Electronic Supplementary Material (ESM)) was performed to determine the lattice parameters of $(Ti_{1-x}Zr_x)_2AlC$. Ti_2AlC (ICDD No. 00-029-0095), α-Ti (ICDD No. 04-002-5207), Ti_3Al (ICDD No. 04-004-2732), TiAl (ICDD No. 04-006-6741) and Zr_3Al_2 (ICDD No. 04-001-3327) were used as initial structural models. The specific parameters are listed in Table S1 in the ESM. Table 1 presents the refinement results, including the lattice parameters and grain sizes. The Zr contents in $(Ti_{1-x}Zr_x)_2AlC$ were determined by GDOES as mentioned later. As x in $(Ti_{1-x}Zr_x)_2AlC$ increased from 0.05 to 0.18, the lattice parameter a monotonically increased from 3.045 to 3.077 Å, and the parameter c increased from 13.656 to 13.702 Å. These parameters were compared with those from experimental and calculated results reported in the literature (Fig. 1(c)) [19,22]. They were very close to the literature values and were only slightly smaller, probably due to residual compressive stress and measurement error. Moreover, they increased linearly with increasing Zr content x, and the rates of increase were highly consistent with those reported in the literature. Increasing the Zr content led to a reduction in the c/a ratio, which is a typical characteristic of the substitution of Zr with a larger atomic size for Ti at the M-site [32]. The grain size of $(Ti_{1-x}Zr_x)_2AlC$ extracted from Rietveld refinement was maintained at approximately 12 nm regardless of the Zr content.

The residual stress (σ_r) of the coatings measured via XRD (Table 1) was lower than that of general ceramic coatings prepared via magnetron sputtering, which can be attributed to the annealing process, which releases the stress. The thermal stress (σ_t) derived from the coefficient of thermal expansion (CTE) mismatch between the coating and substrate can be estimated via Eq. (5) [33]:

$$\sigma_t = \Delta\alpha\Delta T\left(\frac{E}{1-\nu}\right) \quad (5)$$

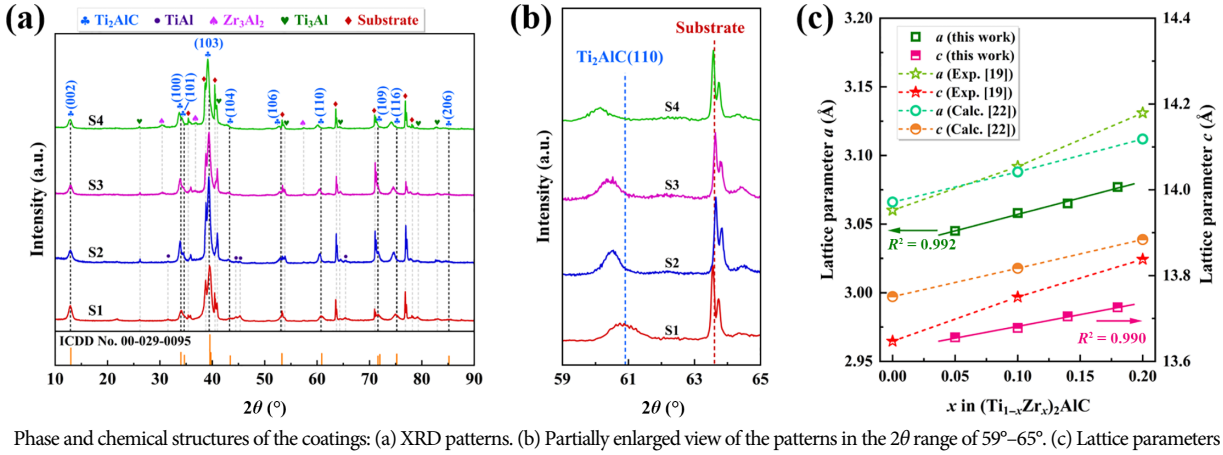

Fig. 1 Phase and chemical structures of the coatings: (a) XRD patterns. (b) Partially enlarged view of the patterns in the 2θ range of 59°–65°. (c) Lattice parameters a and c as functions of the Zr content (x): comparison between this work and other reliable data reported in Refs. [19] and [22].

where $\Delta\alpha$ is the difference between the CTE of the coating (8.8×10^{-6} K^{-1}, derived from the CTE of Ti_2AlC) and the substrate (10.8×10^{-6} K^{-1}, an average value of Ti–6Al–4 V from 25–750 °C [34]), and ΔT is the temperature decrease after cooling from the holding temperature (750 °C) to room temperature. The σ_t was approximately −420 MPa, as calculated via Eq. (5). This value is slightly larger than the σ_r, indicating that the σ_r mainly originated from the σ_t. The growth stress generated by deposition and the phase transition stress generated by crystallization were essentially eliminated by the annealing process.

XPS analysis was performed to provide insight into the chemical compositions and bonding states in the surface region. Figures 2(a)–2(e) show the core-level spectra of Ti 2p, Zr 3d, Al 2p, C 1s, and O 1s, respectively. All the samples exhibited similar chemical components consisting of carbides and oxides, as determined by peak fitting via a GL(30) function, which revealed symmetric peak shapes. Ti in the surface region was identified as oxide TiO_2, TiO_{2-x}, oxycarbide TiO_xC_y, and carbide TiC on the basis of the Ti $2p_{3/2}$ peaks at 458.2–458.4, 456.7–457.1, 455.5–455.8, and 454.2–454.7 eV, respectively. Owing to the vacuum annealing process, the oxygen deficiency led to the formation of substoichiometric oxides, manifesting as a peak with a lower binding energy in the Ti 2p spectra [35]. The peaks assigned to TiO_xC_y imply slight oxidation of the carbides, as evidenced by their higher binding energy than the TiC peaks. Zr and Al were identified as ZrO_2 and Al_2O_3, respectively, on the basis of the Zr $3d_{5/2}$ peaks at 182.1–182.4 eV and the Al 2p peaks at 73.9–74.2 eV. In addition, trace amounts of substoichiometric oxides and carbides of Zr were also identified from peaks of lower binding energy in the Zr 3d spectra, particularly in the coatings with high Zr contents. The C 1s spectra were deconvolved into three components assigned to TiC at 281.4–281.7 eV, TiO_xC_y at 282.5–282.7 eV, sp^3 C–C bonds at 284.8 eV and C–O bonds at 286.7 eV. The latter two originated from surface contamination of the samples exposed to the atmosphere. The O 1s spectra revealed two primary components of TiO_2/ZrO_2 at 530.6 eV and Al_2O_3 at 531.3 eV. Notably, TiO_2 and ZrO_2 were not further distinguished because of the very close binding energy between them [36]. According to the evolution of the O 1s peak intensity, Al_2O_3 gradually decreased while TiO_2/ZrO_2 increased with increasing Zr content.

The composition profiles along the depth direction were obtained via GDOES (Fig. S2 in the ESM). All the coatings were divided into three regions: the outermost O-containing surface layer, the MAX phase matrix layer, and the interlayer adjacent to the substrate. The O content gradually decreased in the O-containing layer, showing typical features of inward oxygen diffusion. In contrast to the observation of hierarchical Al_2O_3 and TiO_2 formed on the surface of Ti_2AlC coatings by oxidation in air [37–39], all the constituent elements were visible in the O-containing layers with noticeable concentrations for the $(Ti_{1-x}Zr_x)_2AlC$ coatings obtained under vacuum annealing conditions. Notably, the Al content exhibited a saltation within the O-containing layer, especially in high-Zr coatings (S3 and S4), suggesting the presence of sublayers with distinct structures. Moreover, increasing the Zr content increased the thickness of the O-containing layer, mainly because of the high affinity between Zr and O. The positions of the $TiAl_x$ interlayer were primarily estimated on the basis of the compositions and cross-sectional SEM images (Fig. S3 in the ESM). The semiquantitative compositions of the $(Ti_{1-x}Zr_x)_2AlC$ matrix layers extracted from the corresponding regions in the profiles are listed in Table 2. The x values were 0.05, 0.1, 0.14, and 0.18 for the S1–S4 coating samples, respectively. As expected, increasing the power of the Zr target promoted C deposition and Al resputtering, resulting in an increase in the C content and a decrease in the Al content [40]. Excess C was generally detrimental to the formation of Ti_2AlC but had a negligible effect on the synthesis of $(Ti_{1-x}Zr_x)_2AlC$ in this work, which can be attributed to the enhanced structural stability of the solid solution structure for MAX phases [41,42]. A similar composition trend was also observed in the O-containing layer, where the Al content gradually decreased with increasing Zr content.

The microstructures of different regions in the $(Ti_{0.82}Zr_{0.18})_2AlC$ coating were investigated via TEM characterization. The bright-field (BF) image (Fig. 3(a)) displays a hierarchical structure. The

Table 1 Lattice parameters (a and c), c/a ratios, and grain sizes of $(Ti_{1-x}Zr_x)_2AlC$ obtained via Rietveld refinement and the σ_r measured via the XRD-sin$^2\psi$ method

Sample	a (Å)	c (Å)	c/a	Grain size (nm)	σ_r (MPa)
S1: $(Ti_{0.95}Zr_{0.05})_2AlC$	3.045	13.656	4.487	12	−335±52
S2: $(Ti_{0.9}Zr_{0.1})_2AlC$	3.058	13.679	4.473	12	−392±70
S3: $(Ti_{0.86}Zr_{0.14})_2AlC$	3.065	13.703	4.471	11	−294±58
S4: $(Ti_{0.82}Zr_{0.18})_2AlC$	3.077	13.726	4.461	13	−391±43

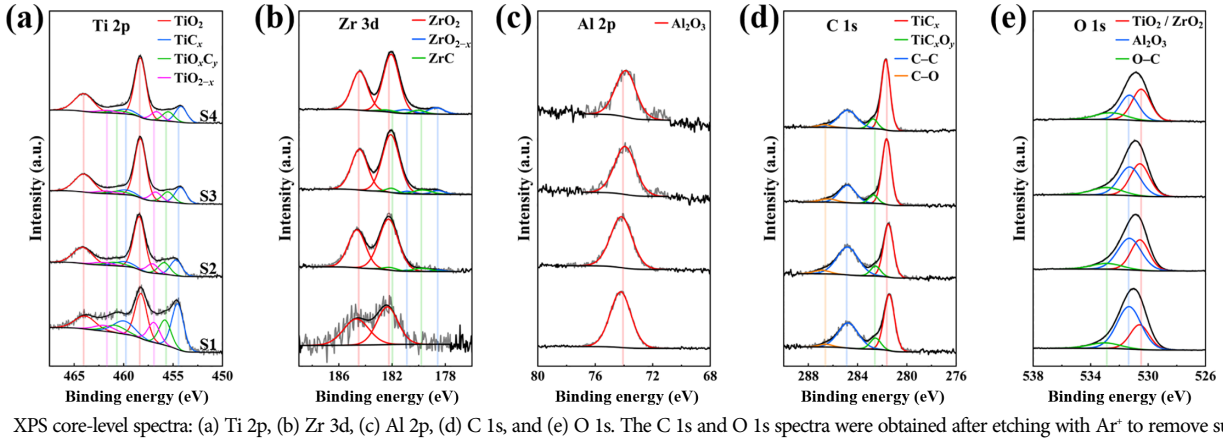

Fig. 2 XPS core-level spectra: (a) Ti 2p, (b) Zr 3d, (c) Al 2p, (d) C 1s, and (e) O 1s. The C 1s and O 1s spectra were obtained after etching with Ar^+ to remove surface contaminants. The gray lines denote the experimental results, and the dark lines denote the fitting results. The Ti 2p and Zr 3d spectra have two spin-orbit splitting peaks for each component: the $2p_{3/2}$ peak at lower binding energies and the $2p_{1/2}$ peak at higher binding energies. For clarity, the spectra of the same element were normalized.

surface region exhibited poor crystallinity. Energy dispersive spectroscopy (EDS) mapping (Fig. 3(b)) revealed that the surface layer was enriched in O and depleted in Al. By comparing the EDS mapping with the compositional depth profiles (Fig. S2(d) in the ESM), it can be reasonably inferred that the surface layer in the TEM images corresponds to the upper portion of the O-containing layer in the GDOES profile. The region below the low-crystalline layer, which had a measurable O content and an increasing Al content with depth, corresponds to the lower portion of the O-containing layer. The high resolution TEM (HRTEM) image (Fig. 3(c)) shows that the surface layer contained ultrafine nanocrystals with a grain size of ~3 nm and amorphous phases. The TiC phase was identified on the basis of the selected area electron diffraction (SAED) pattern obtained from the surface region (Fig. 3(c)). The interplanar spacing measured in the grains was 0.43 nm, corresponding to the (100) plane of TiC. Since no other crystalline phase was present except for TiC within the surface layer, oxides, including TiO_2, Al_2O_3, and ZrO_2, existed

Table 2 Compositions of MAX phase matrix layers (Unit: at%)

Sample	Ti	Zr	Al	C	Zr / (Ti + Zr)
S1	39.9	2.3	32.1	25.7	0.05
S2	37.8	4.2	30.8	27.2	0.10
S3	34.0	5.3	26.7	33.9	0.14
S4	32.3	6.9	26.7	34.1	0.18

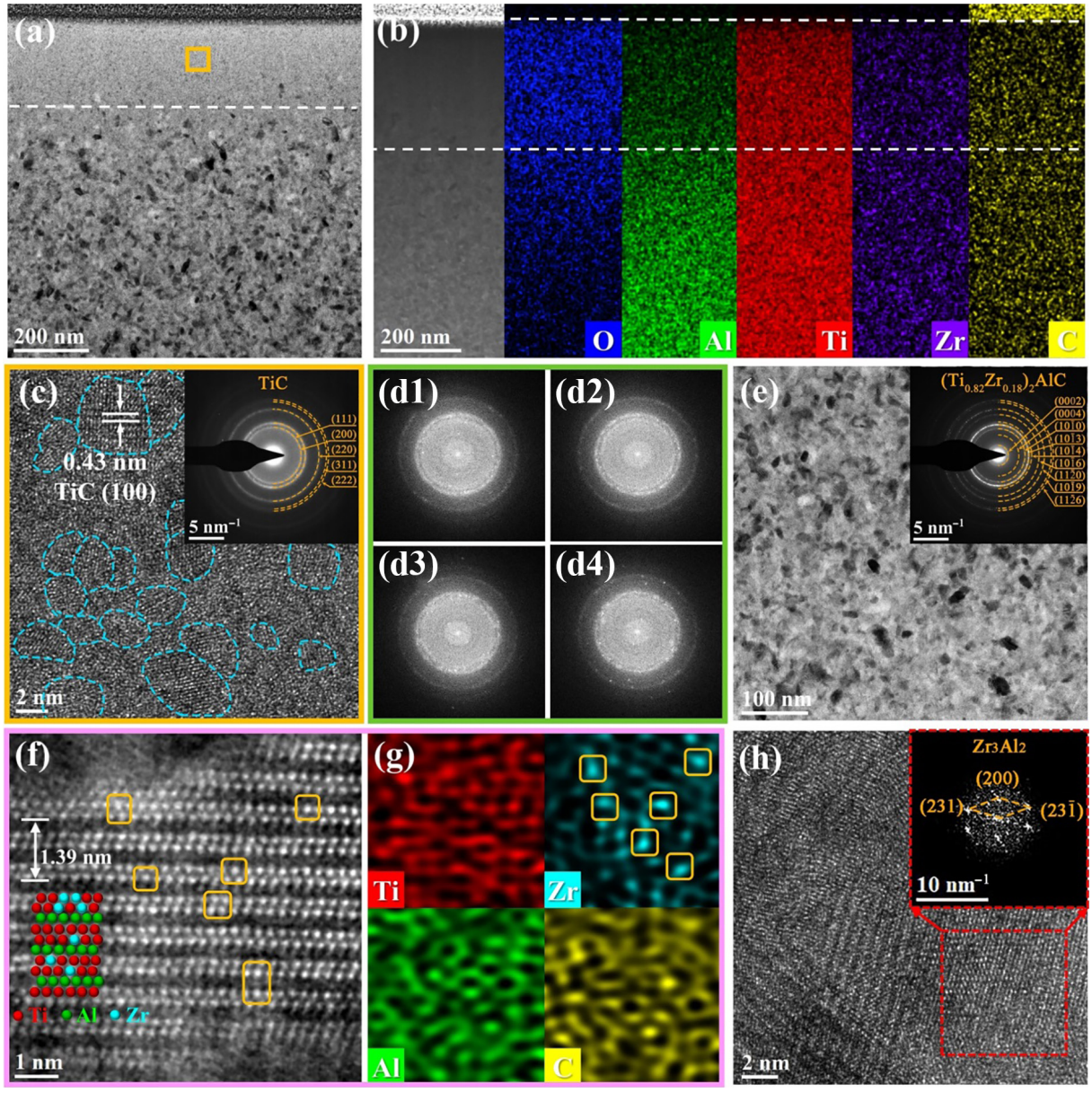

Fig. 3 Cross-sectional TEM micrographs of the $(Ti_{0.82}Zr_{0.18})_2AlC$ coating. (a) BF image. (b) EDS mapping images. (c) HRTEM image of the region in surface layer and corresponding SAED pattern. Blue dotted lines indicate crystalline grains. (d1–d4) FFT images along the depth direction within the surface layer. (e) BF image of the $(Ti_{0.82}Zr_{0.18})_2AlC$ layer and corresponding SAED pattern. (f) Atomic-resolution HAADF image of $(Ti_{0.82}Zr_{0.18})_2AlC$ and (g) EDS mapping images. (h) HRTEM and FFT images showing the presence of Zr_3Al_2.

in an amorphous form. Owing to the large capture size of SAED (200 nm), fast Fourier transform (FFT) analysis was performed in 50 nm × 50 nm regions to investigate the structural evolution across the amorphous-nanocrystalline oxidation layer along the depth direction (Figs. 3(d1)–3(d4)). From top to bottom, the rings became discontinuous (Fig. 3(d3)), and multiple distinct diffraction spots emerged (Fig. 3(d4)), indicating a gradual increase in crystallinity.

Figure 3(e) presents a BF image and a corresponding SAED pattern, which confirms the presence of single-phase equiaxed $(Ti_{0.82}Zr_{0.18})_2AlC$, indicating that other phases identified by XRD were likely located in the interlayer or substrate. Figure S4 and Table S2 in the ESM present the TEM images and EDS compositions of the interface region between the coating and substrate. The interlayer was mainly composed of TiAl (Fig. S4(c) in the ESM), and the substrate contained Ti_3Al (Fig. S4(d) in the ESM). The compositional analysis of these two regions demonstrates general consistency with the identified phases. Compared with the nominal content, the substrate region adjacent to the interlayer had an elevated Al content, confirming the formation of Ti_3Al through Al diffusion from the TiAl interlayer into the substrate. Therefore, the signals corresponding to Ti_3Al and TiAl in the XRD patterns can be attributed to the interlayer and substrate. No Zr_3Al_2 was detected by SAED, probably because of its very low content. Figure S5 in the ESM shows a TEM dark-field (DF) image and the size distribution of MAX phase grains derived from the image. The average size was 12 nm, which is in excellent agreement with the results obtained from the XRD data. The atomic arrangement of $(Ti_{0.82}Zr_{0.18})_2AlC$ was revealed via high-angle annular dark-field (HAADF) imaging using C_S-corrected TEM, with the electron beam parallel to the $[11\bar{2}0]$ direction (Fig. 3(f)). The contrast of an atom in a HAADF image is related to its atomic number, where heavier atoms exhibit higher contrast. It is evident that $(Ti_{0.82}Zr_{0.18})_2AlC$ had a representative sandwich structure of 211 MAX phases where two layers of M-site atoms (Ti or Zr) and one layer of A-site atoms (Al) were stacked alternately along the [0001] direction. C atoms were invisible due to their low diffraction intensity. The lattice parameter c was measured to be 1.39 nm, which is basically in accordance with the value from XRD. The orange boxes in Fig. 3(f) show the atoms larger than the surrounding ones among the M-site atoms, indicating the occupancy of Zr atoms at the M-site. The EDS mapping images (Fig. 3(g)) further support this point: Ti, Al, and C exhibited relatively uniform distributions, whereas Zr was enriched in the highlighted regions, corresponding to the marked positions in the HAADF image. In addition to $(Ti_{0.82}Zr_{0.18})_2AlC$, Zr_3Al_2 was also identified by HRTEM (Fig. 3(h)), suggesting that its content was below the detection limit of SAED. These observations demonstrate that the hierarchical coating consisted of nanocrystalline $(Ti_{0.82}Zr_{0.18})_2AlC$ solid solution with an amorphous-nanocrystalline oxidation layer on the surface. A continuous microstructural transition was observed from the oxidation layer to the underlying $(Ti_{0.82}Zr_{0.18})_2AlC$ without distinct boundaries separating the two regions (Fig. 3(a)), resulting in a gradient structure from low to high crystallinity and ultimately to complete crystallization with larger grains.

3.2 Mechanical properties

The mechanical properties of the hierarchical $(Ti_{1-x}Zr_x)_2AlC$ coatings were evaluated via nanoindentation. Figure S6(a) in the ESM shows the load–depth curves from the nanoindentation tests performed with a Berkovich indenter. When $x \geq 0.1$, the load clearly increased faster with increasing depth than that of the $(Ti_{0.95}Zr_{0.05})_2AlC$ coating. However, the coatings with $x \geq 0.1$ exhibited similar loading and unloading behaviors, suggesting comparable deformation resistance. The elastic recovery index (R_E), which is calculated as the ratio of unloading work to total work, can be used to evaluate the plastic deformation capacity. As the Zr content increased, R_E slightly increased and remained constant. Generally, a higher R_E indicates that more strain energy is mitigated by reversible elastic deformation, favoring strong resistance to plastic deformation and crack propagation [43]. Figure 4(a) shows the hardness (H) and elastic modulus (E) extracted from the load–depth curves. As x increased from 0.05 to 0.1 in the $(Ti_{1-x}Zr_x)_2AlC$ coating, the hardness significantly increased from 16.5±0.3 to 18.6±0.3 GPa and subsequently slightly increased to 19.2±0.2 GPa for x = 0.18. Considering the negligible change in grain size for x = 0.05–0.18, more substitution of Zr atoms for Ti atoms in $(Ti_{1-x}Zr_x)_2AlC$ was likely the vital factor contributing to the hardness increase. Nevertheless, the rate of hardness increase slowed down when the Zr content reached a relatively high level ($x \geq 0.1$). The H/E and H^3/E^2 ratios, which are associated with the elastic strain limit and yield limit, respectively [44], also tended to increase (Fig. 4(b)). Considering their hardness and elastic properties, the $(Ti_{1-x}Zr_x)_2AlC$ coatings with higher Zr contents ($x \geq 0.1$) were less prone to deformation and cracking, indicating improved toughness.

Nanoindentation tests with a cube-corner indenter were

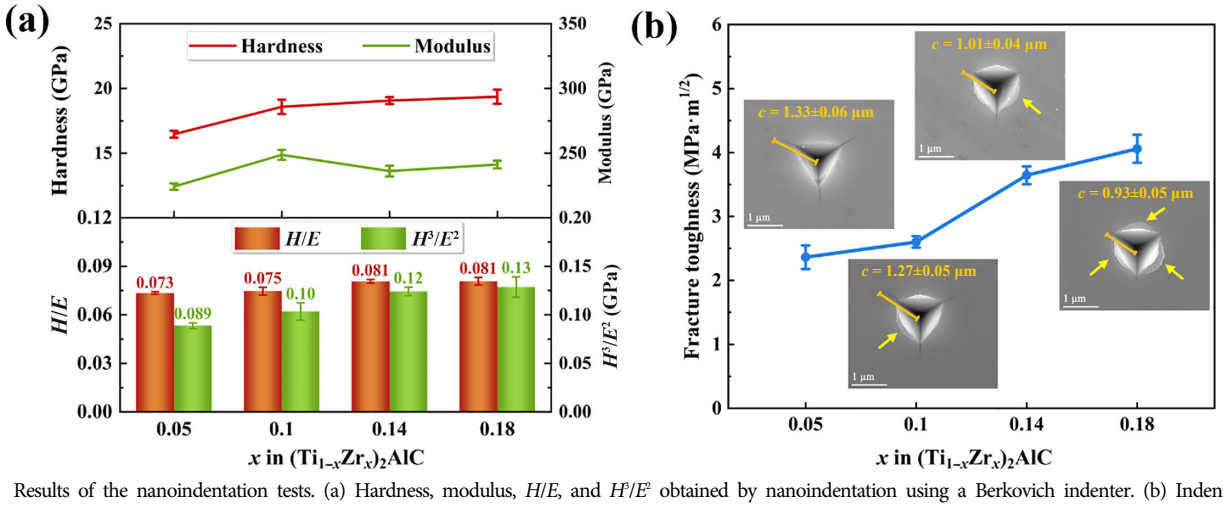

Fig. 4 Results of the nanoindentation tests. (a) Hardness, modulus, H/E, and H^3/E^2 obtained by nanoindentation using a Berkovich indenter. (b) Indentation morphologies, average total crack lengths c from the indentation to the crack tip, and calculated fracture toughness obtained by nanoindentation using a cube-corner indenter. The segments indicate the range of total crack lengths (c), and the arrows indicate the shear steps.

performed to further evaluate the fracture toughness of the coatings. All the coatings revealed nearly overlapping load–depth curves at a peak load of 20 mN, along with converging and lower R_E values (Fig. S6(b) in the ESM). This phenomenon indicates similar plastic work against large presses. An inconspicuous strain burst behavior, also called "pop-in", emerged on the loading curve of the $(Ti_{0.82}Zr_{0.18})_2AlC$ coating. However, it showed that the depth increased more rapidly with increasing load, unlike typical pop-in, which exhibited a sudden jump in depth at a certain load. Pop-in is usually associated with certain special deformation behaviors, such as plastic flow and cracking [45]. Fracture toughness was calculated on the basis of the average length of radial cracks from the indentation center to the crack tip (Fig. 4(b)). Increasing the Zr content in the $(Ti_{1-x}Zr_x)_2AlC$ coatings improved the fracture toughness. In particular, the highest toughness reached 4.1±0.2 MPa·m$^{1/2}$ for the $(Ti_{0.82}Zr_{0.18})_2AlC$ coating. The contribution of residual compressive stress was subtracted. Considering the nearly identical elastic and plastic work in cube-corner nanoindentation tests, the improvement in fracture toughness can be attributed primarily to the increased plastic deformability. The evidence is that the pile-ups around the indentation became more distinct, as shown in the SEM images (Fig. 4(b)), presenting unambiguous plastic flow of the volume displaced by the indenter. Specifically, the $(Ti_{0.95}Zr_{0.05})_2AlC$ coating exhibited slight bumps around the indentation edges, whereas the coatings with $x \geq 0.1$ presented pronounced petal-like pile-ups, indicating the presence of shear steps. Shear steps are typically accompanied by pop-ins on the load–depth curve [46], and Fig. S6(b) in the ESM shows this phenomenon. As the Zr content increased, more shear steps formed. Combining the curves and indentation morphologies, increasing the Zr content improved the plasticity of the coatings, thereby impeding the propagation of radial cracks and substantially improving the fracture toughness.

Micropillar compression tests were performed to study the uniaxial compressive behavior of the coatings. Compared with nanoindentation, micropillar compression more accurately reflects distinct elastic and plastic deformation behaviors and quantifies the strength and ductility of coatings. The $(Ti_{0.9}Zr_{0.1})_2AlC$ and $(Ti_{0.82}Zr_{0.18})_2AlC$ coatings were selected for testing. Figure S7(a) in the ESM shows their pristine uncompressed morphologies and sizes. Extremely small taper angles were conducive to more accurate calculations of stress and strain. Figure 5(a) displays their true stress–strain curves. After a nonlinear contact process due to the surface roughness of the coatings and indenter, linear elastic behavior was observed. The elastic modulus, defined as the slope of the curve in the elastic stage, was 192 GPa for the $(Ti_{0.9}Zr_{0.1})_2AlC$ coating and 182 GPa for the $(Ti_{0.82}Zr_{0.18})_2AlC$ coating. Although the modulus values obtained in this manner were different from those determined by nanoindentation due to different test principles, the observed trends were consistent. Since no obvious yield behavior appeared on the curves, the yield strength was defined as the stress where 0.2% plastic strain occurs beyond the elastic stage. Although two samples exhibited brittle fracture, the $(Ti_{0.82}Zr_{0.18})_2AlC$ coating underwent a short stage of plastic deformation according to the stress–strain curves. However, even immediately before fracture, no visible plastic deformation was observed (Fig. S7(c) in the ESM). Given the strain bursts (pop-ins) observed in the plastic stage, which were also present in nanoindentation and related to the shear steps around the indentation, the observation is likely associated with shear deformation at the top. The morphology after fracture (Fig. S7(b) in the ESM) shows that minor plastic deformation occurred in the top region with multiple shear bands. Several inclined large cracks below indicate that shear cracking was the dominant failure mode.

The strength, ductility and toughness of the two coatings are compared in Fig. 5(b). The $(Ti_{0.82}Zr_{0.18})_2AlC$ coating had a lower yield strength of 7.9 GPa but a higher ultimate compressive strength of 9.8 GPa due to strain hardening. The presence of plastic deformation endowed the $(Ti_{0.82}Zr_{0.18})_2AlC$ coating with greater ductility, as indicated by a fracture strain of 9.7%. The contributions of the elastic and plastic components to ductility can be represented by the elastic strain (ε_e) and plastic strain (ε_p), respectively (Eqs. (6) and (7)):

$$\varepsilon_e = \frac{\sigma_f}{E_{MC}} \tag{6}$$

$$\varepsilon_p = \varepsilon_f - \varepsilon_e \tag{7}$$

where σ_f is the stress at the fracture, E_{MC} is the elastic modulus obtained in compression tests, and ε_f is the fracture strain (Fig. 5(a)). The elastic strain and plastic strain were 4.9% and 0.2%, respectively, for the $(Ti_{0.9}Zr_{0.1})_2AlC$ coating, whereas they were 5.4% and 1.8%, respectively, for the $(Ti_{0.82}Zr_{0.18})_2AlC$ coating. Since the elastic component contributed comparably to ductility, enhanced plastic deformability contributed to greater ductility in

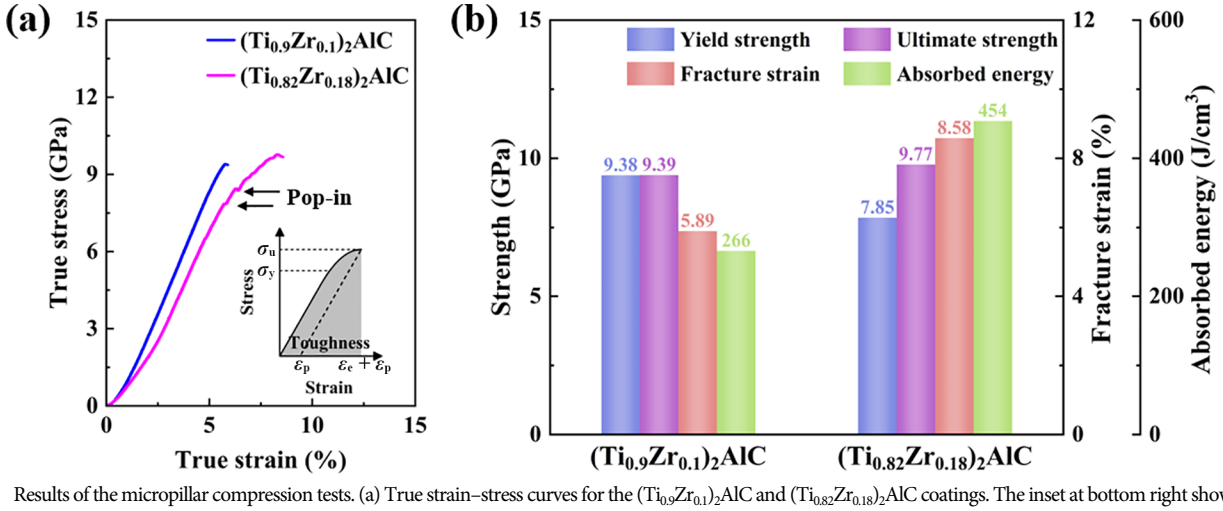

Fig. 5 Results of the micropillar compression tests. (a) True strain–stress curves for the $(Ti_{0.9}Zr_{0.1})_2AlC$ and $(Ti_{0.82}Zr_{0.18})_2AlC$ coatings. The inset at bottom right shows the yield strength (σ_y), ultimate compressive strength (σ_u), elastic strain (ε_e), plastic strain (ε_p), and toughness. (b) Yield strength, ultimate compressive strength, fracture strain (ductility), and energy absorbed up to fracture (toughness) extracted from the true strain–stress curves.

the $(Ti_{0.82}Zr_{0.18})_2AlC$ coating. Toughness is a comprehensive measure of strength and ductility and is typically evaluated by the energy absorbed up to fracture in compression tests, which is calculated from the area under the stress–strain curve. Owing to its higher strength and ductility, the $(Ti_{0.82}Zr_{0.18})_2AlC$ coating absorbed more energy before fracture, thus possessing a greater toughness than the $(Ti_{0.9}Zr_{0.1})_2AlC$ coating. This result is consistent with the fracture toughness measured via nanoindentation tests.

3.3 Microstructure evolution and deformation mechanisms

To elucidate the effect of the microstructure on the mechanical properties, the cross-section of the indentation on the $(Ti_{0.82}Zr_{0.18})_2AlC$ coating was examined via TEM. A load of 50 mN was employed to generate greater plastic deformation for observation and analysis. Figure 6(a) shows the position where the TEM lamella was extracted and the scanning TEM (STEM) image of the indentation cross-section. In addition to the radial crack at the indentation corner, two additional cracks were observed: a median crack directly beneath the indentation center along the loading direction and a lateral crack at the bottom right of the indentation, representing axial splitting by tensile stress and shear cracking, respectively. Both cracks initiated at the plastic zone boundary. Compared with axial splitting, shear cracking is generally somewhat ductile [47]. This is consistent with the observation that the median crack was longer than the lateral crack and even propagated into the substrate.

The remarkable plastic deformability of the oxidation layer is clearly presented in Fig. 6(b), with a gradual decrease in layer thickness toward the indentation center, from ~250 nm in the

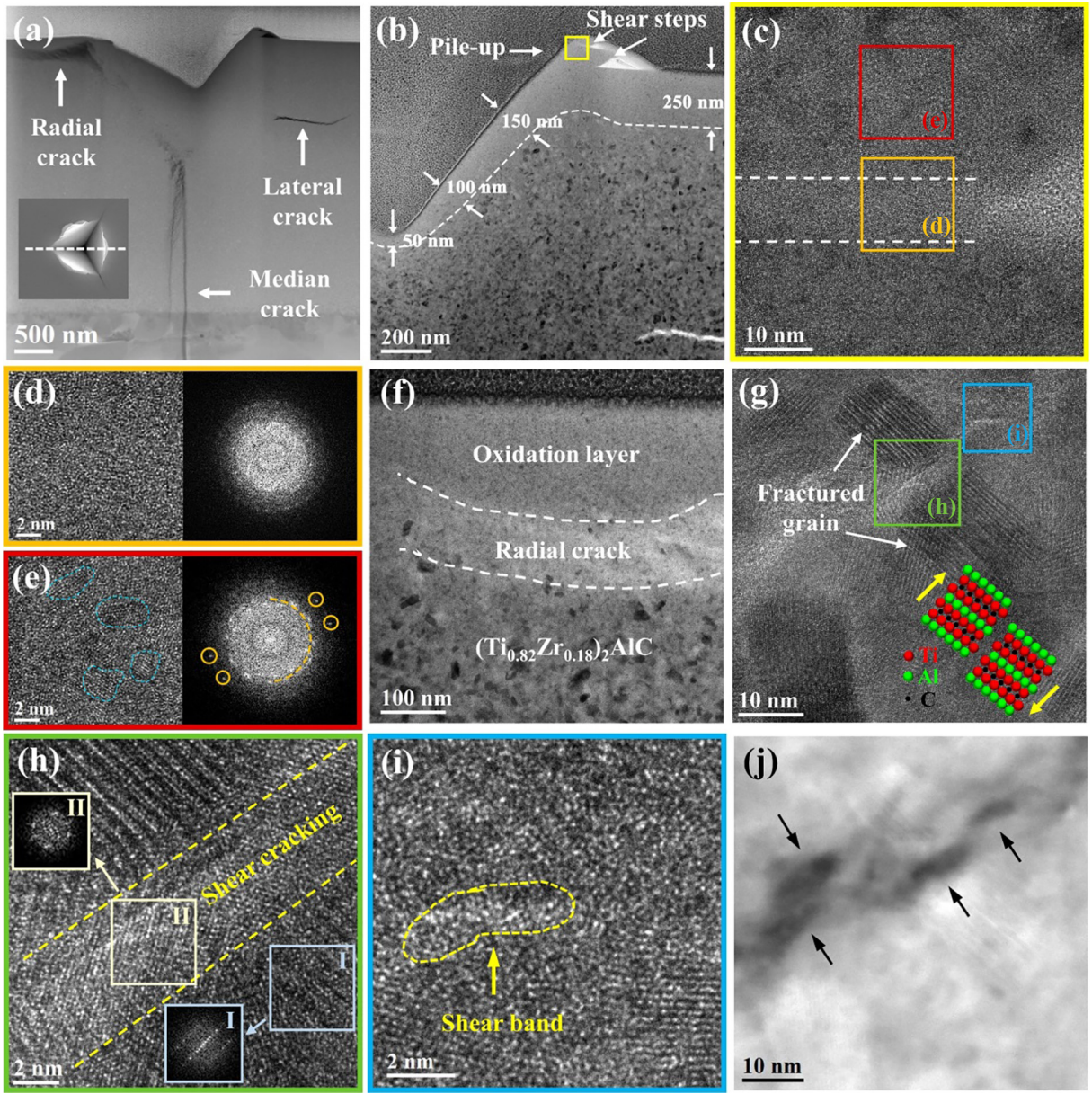

Fig. 6 Cross-sectional TEM micrographs of the indentation on the $(Ti_{0.82}Zr_{0.18})_2AlC$ coating, produced by a cube-corner indenter under a 50 mN load: (a) STEM image showing an overview of the indentation cross section. The inset at bottom left indicates the cutting position of the TEM sample. (b) BF image in the indentation region. (c) HRTEM image of the area marked in (b), along with enlarged HRTEM images and corresponding FFT images in (d) core zone and (e) peripheral zone of a shear band. (f) BF image showing the tip region of the radial crack. (g) HRTEM image of the tip region of the lateral crack, along with (h, i) enlarged views. (j) HAADF image. The arrows show dark regions denoting well-developed shear bands or microcracks.

undeformed zone to ~50 nm in the zone directly beneath the indentation center. Plastic flow under high stress resulted in a distinct pile-up with a height of 120 nm. A series of shear steps were directly observed at the pile-up region without any cracks. This corresponds to the petal-like morphology of the pile-ups in the top view of the indentation (Fig. 4(b)) and produced a pop-in phenomenon on the loading curve (Fig. S6(b) in the ESM). An enlarged view of the shear steps (Fig. 6(c)) shows the presence of a shear band, whose core zone was a narrow stripe with an amorphous structure, as illustrated by the HRTEM image and FFT pattern (Fig. 6(d)). In contrast, the peripheral zone was partially crystalline, as evidenced by the presence of grains in the HRTEM image and diffraction spots in the FFT image (Fig. 6(e)). The strain energy dissipated through homogeneous plastic flow and shear banding, thereby effectively suppressing crack initiation and propagation. Furthermore, crack deflection also contributed to toughness. Figure 6(f) shows the tip structure of the radial crack that was discontinuous and only present inside the coating. This occurred because the TEM lamella position was slightly offset from the crack center, and the crack deflection segment during downward propagation was captured within the lamella.

For the $(Ti_{0.82}Zr_{0.18})_2AlC$ layer, the portion in the plastic zone exhibited minor plastic deformation (Fig. 6(b)), whereas cracks initiated at the plastic zone boundary and subsequently propagated along the loading direction as the median crack or parallel to the surface as the lateral crack. Lateral cracks pose a considerable risk, as they may cause material removal by propagation toward the surface under sharp contact (Fig. 6(a)) [48]. Thus, shear-induced brittle cracking in the MAX phase layer can lead to failure. Figure 6(g) shows that a grain fractured in the direction perpendicular to the base plane, resulting in two staggered segments at the crack tip, along with a corresponding model diagram. This shearing can generate kink bands in bulk MAX phases, which is an important plastic deformation mechanism arising from the movement of dislocation walls [49]. In the $(Ti_{0.82}Zr_{0.18})_2AlC$ coating, however, this kinking was difficult to achieve because of the constrained dislocation motion in such small grains. Note that there were still unbroken crystalline phases in the microcrack (Fig. 6(h)), indicating that microcracks formed preferentially at some positions. Figure 6(i) shows that the microcrack formed by shear banding and amorphization. The STEM image (Fig. 6(j)) clearly shows the microcrack distribution. The black regions were extremely thin, corresponding to well-developed shear bands or microcracks, whereas the moderately dark regions were the initial shear bands. The unstable propagation of shear bands led to their merging and cracking. This result corresponds to that of the compression tests, in which shear bands were concentrated in the top region of the pillars, whereas the main cracks were located in the middle and lower parts (Fig. S7(b) in the ESM). Although $(Ti_{0.82}Zr_{0.18})_2AlC$ appeared more susceptible to cracking, the tough oxidation layer with an amorphous-nanocrystalline structure acted as a stress absorbing layer, thereby compensating for this drawback.

3.4 Discussion

The results of nanoindentation and micropillar compression demonstrated that increasing the Zr content in the $(Ti_{1-x}Zr_x)_2AlC$ coatings increased the hardness and strength as expected, which was attributed to the large lattice mismatch induced by the solid solution of Zr at the M-site. The atomic-resolution HAADF-STEM image and EDS mapping image (Figs. 3(f) and 3(g)) confirmed the formation of a solid solution $(Ti_{1-x}Zr_x)_2AlC$. Nevertheless, this enhancement became slight when the Zr content was high ($x > 0.1$). Since the valence electron concentration of $(Ti_{1-x}Zr_x)_2AlC$ remained constant regardless of the Zr content, lattice expansion reduced the bonding strength and counteracted a portion of the strengthening effect. A theoretical study based on DFT calculations also revealed that the hardness of $(Ti_{1-x}Zr_x)_2AlC$ slightly increased with increasing Zr content [22]. Another strengthening factor is the presence of second phase Zr_3Al_2. The XRD data reveal that increasing the Zr content transformed TiAl into Zr_3Al_2, and the hardness of the latter was far greater than that of the former [50]. Therefore, the formation of the hard phase increased the coating hardness. However, it could increase the driving force for intergranular fracture, thereby reducing toughness [51].

Despite the debate regarding the accuracy of the quantitative analysis of fracture toughness by nanoindentation, the resistance to surface crack propagation was indeed improved, as evidenced by the reduction in crack length from 1.33 μm for the $(Ti_{0.95}Zr_{0.05})_2AlC$ coating to 0.93 μm for the $(Ti_{0.82}Zr_{0.18})_2AlC$ coating (Fig. 4(b)). Under plane stress conditions, the plastic zone size (r_p) at the crack tip can be estimated by Eq. (8) [52]:

$$r_p = \frac{1}{2\pi}\left(\frac{K_I}{\sigma_y}\right)^2 \tag{8}$$

where K_I is the stress intensity factor calculated via Eq. (2), and σ_y is the yield strength. For the $(Ti_{0.9}Zr_{0.1})_2AlC$ and $(Ti_{0.82}Zr_{0.18})_2AlC$ coatings, the r_p was 12 and 48 nm, respectively. In the MAX phase layer, the r_p was comparable to the grain size of $(Ti_{0.9}Zr_{0.1})_2AlC$ but larger than that of $(Ti_{0.82}Zr_{0.18})_2AlC$. However, according to the results of the compression tests, the micropillar still suddenly collapsed, indicating that the larger plastic zone was insufficient to prevent unstable crack propagation within the $(Ti_{0.82}Zr_{0.18})_2AlC$ layer. In the oxidation layer, the r_p was much larger than the grain size, indicating that the crack propagation was shielded through synergetic plastic deformation of multiple grains and amorphous phases [52]. As the Zr content increased, a thicker oxidation layer could accommodate a fully developed plastic zone without any truncation at the interface and prevent surface cracks from entering brittle $(Ti_{1-x}Zr_x)_2AlC$ below, thus improving the overall fracture toughness of the hierarchical coating [53].

It is clear that the amorphous-nanocrystalline structure in the oxidation layer is crucial to high toughness. When the grain size is small enough, e.g., less than 10 nm, shear banding replaces dislocation slip as the primary deformation mechanism [16,52], indicating that the TiC nanocrystals in the oxidation layer possess plastic deformability via shear banding. This facilitates the synergetic deformation of the nanocrystalline and amorphous phases, since shear banding is also the main deformation mechanism of the amorphous phases. In amorphous oxides, O vacancies forming due to O deficiency during vacuum annealing, and stress concentrations at amorphous-nanocrystalline interfaces increased the free volume and promoted the formation of shear bands that accommodated strain [54–56]. The amorphous-nanocrystalline interfaces served as barriers to unstable propagation of shear bands, promoting the activation of subshear bands and homogeneous plastic deformation, thereby alleviating stress concentrations and postponing crack initiation and propagation [5,57]. This is supported by the observation of only one main shear band in the severely deformed region of the oxidation layer (Figs. 6(b) and 6(c)). Therefore, despite the intrinsic brittleness of oxides and carbides, the oxidation layer comprising amorphous oxides and nanocrystalline carbides exhibited remarkably high toughness. Furthermore, additional strain hardening emerged owing to stress gradients induced by the

gradient structure from the oxidation layer to the $(Ti_{1-x}Zr_x)_2AlC$ layer, further increasing the ductility and toughness of the hierarchical coatings [58]. The structural gradient stemmed from the compositional gradient, specifically a gradual reduction in O and a gradual increase in other elements along the depth direction.

The thickening of the oxidation layer, another vital factor for toughness enhancement, can be attributed to the decrease in the Al_2O_3 content in the oxidation layer with increasing Zr content (Fig. 2(e)). During vacuum annealing, the oxygen partial pressure was tremendously low, leading to preferential oxidation of the elements with high oxygen affinity. According to the standard Gibbs free energy ΔG associated with the oxidation reactions at 750 °C for TiO_2, ZrO_2, and Al_2O_3 (obtained from the database in the HSC software) (Reactions (9)–(11)):

$$Ti(s) + O_2(g) = TiO_2(s) \quad \Delta G = -758.6\ kJ/mol \tag{9}$$

$$\frac{4}{3}Al(s) + O_2(g) = \frac{2}{3}Al_2O_3(s)\ \Delta G = -902.6\ kJ/mol \tag{10}$$

$$Zr(s) + O_2(g) = ZrO_2(s) \quad \Delta G = -905.3\ kJ/mol \tag{11}$$

Al and Zr have higher affinities with O than with Ti, so O preferentially combined with Al and Zr to produce Al_2O_3 and ZrO_2. TiC was the product of $(Ti_{1-x}Zr_x)_2AlC$ losing Al and Zr [59]. However, the high vapor pressure of Al exacerbated its loss in high-temperature and vacuum environments, which promoted the preferential formation of ZrO_2 and prevented the development of a continuous Al_2O_3 scale, thus accelerating the oxidation process. Increasing the Zr content produced more ZrO_2, further suppressing Al_2O_3 formation and accelerating Al loss under vacuum. As a result, protective Al_2O_3 decreased in the oxidation layer, whereas non-protective ZrO_2, TiO_2, and TiC increased. Owing to the relatively low annealing temperature and short holding time, the oxides lacked sufficient time for crystallization and remained amorphous [28,60]. The presence of O vacancies further led to lattice instability and consequential amorphization. With increasing Zr content, larger thickness of the tough oxidation layer led to increased fracture toughness of the coatings. Notably, the oxidation layer is not thick enough for spalling caused by growth stress. Owing to the gradient structure, which improved the physical compatibility on both sides of the interface, the adhesion of the oxidation layer on the $(Ti_{1-x}Zr_x)_2AlC$ layer was strong.

Overall, increasing the Zr content in hierarchical $(Ti_{1-x}Zr_x)_2AlC$ coatings increased the hardness to 19.4 GPa and the fracture toughness to 4.1 MPa·m$^{1/2}$. Figure 7 compares the hardness and fracture toughness of some MAX phases, including pure phases [61–69], solid solutions [70–72], and coatings [17,73]. Since the grain sizes (11–13 nm) were close to the critical size of the transition point from the Hall–Petch relation to the inverse Hall–Petch relation, combined with the solid solution and second phase strengthening effect induced by Zr doping, the $(Ti_{1-x}Zr_x)_2AlC$ coatings in this work had a higher hardness than the MAX phase coatings reported previously. More importantly, the growth of an amorphous-nanocrystalline oxidation layer on the surface substantially improved the overall fracture toughness of the hierarchical coatings, allowing them to retain a fracture toughness approaching the bulk MAX phase level while exhibiting a hardness far greater than that of the bulk materials.

4 Conclusions

In summary, high-hardness and high-toughness hierarchical $(Ti_{1-x}Zr_x)_2AlC$ coatings (x = 0.05–0.18) were fabricated via multitarget magnetron sputtering followed by vacuum annealing. An oxidation layer composed of nanocrystalline carbides and amorphous oxides was formed *in situ* on the coating surface during annealing. The formation of MAX phase solid solutions of Zr at the M-site was confirmed by XRD and atom-resolved TEM analyses. Increasing the Zr content facilitated the growth of the oxidation layer and the formation of second phase Zr_3Al_2. The coatings exhibited comprehensive improvements in hardness, compressive strength, ductility and fracture toughness with increasing Zr content. The enhanced hardness and strength resulted primarily from solid solution strengthening and second phase strengthening, both of which constrained dislocation motion and shear deformation. More importantly, the amorphous-nanocrystalline oxidation layer exhibited extraordinary plastic deformability and crack resistance. Amorphous-nanocrystalline interfaces impeded the unstable propagation of shear bands and promoted homogeneous plastic deformation. The gradient structure provided additional strain hardening capacity. These mechanisms compensate for the low ductility of $(Ti_{1-x}Zr_x)_2AlC$, resulting in high fracture toughness of the hierarchical coatings.

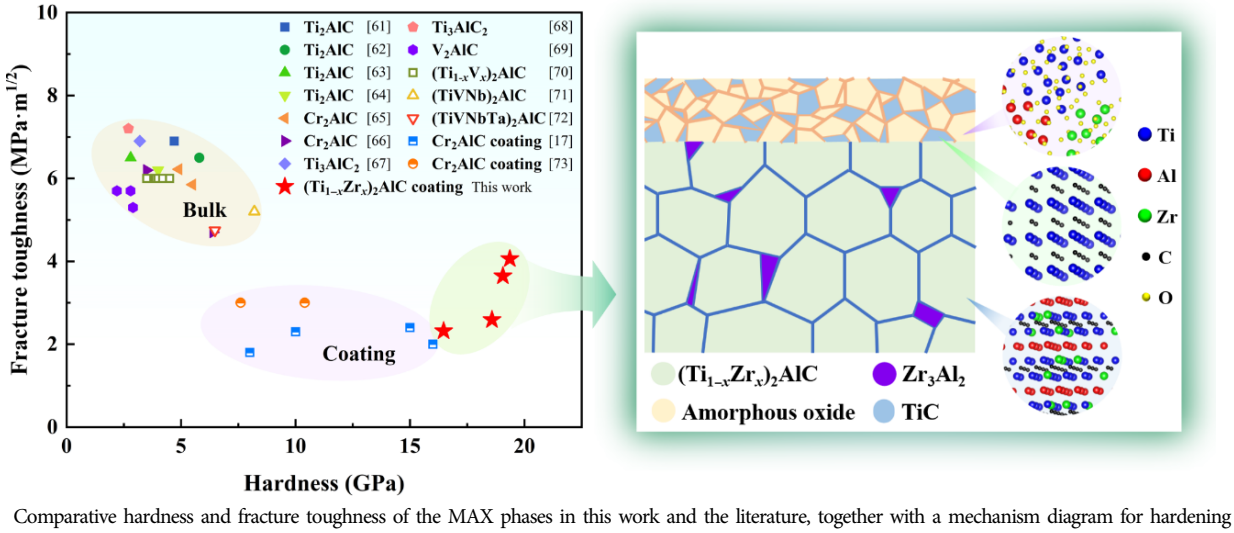

Fig. 7 Comparative hardness and fracture toughness of the MAX phases in this work and the literature, together with a mechanism diagram for hardening and toughening.

Accelerated oxidation driven by the strong Zr–O affinity and high volatility of Al during vacuum annealing thickened the tough oxidation layer. Consequently, the optimized $(Ti_{0.82}Zr_{0.18})_2AlC$ coating reached a hardness of 19.4 GPa and a fracture toughness of 4.1 MPa·m$^{1/2}$. This research proposes a novel strategy based on alloying and vacuum oxidation to effectively resolve the conventional trade-off between toughness and hardness, providing a viable route for designing mechanically robust MAX phases or other ceramic coatings.

Acknowledgements

This work was financially supported by the National Key R&D Program of China (No. 2024YFB3816500), the National Natural Science Foundation of China (Nos. U22A20111 and 52571117), and the Natural Science Foundation of Zhejiang Province (No. LR26E010004).

Availability of data and materials

The data that support the findings of this study are available from the corresponding author upon reasonable request.

Competing interests

The authors have no competing interests to declare that are relevant to the content of this article.

Electronic Supplementary Material

Supplementary material is available in the online version of this article at https://doi.org/10.26599/JAC.2025.9221201.

References

[1] Tan ZY, Wu X, Zhu W, *et al.* Ultra-high hardness induced by W precipitation within Ta–Hf–W–C ultra-high temperature ceramic coatings. *J Eur Ceram Soc* 2022, **42**: 6288–6294.

[2] Kou HN, Lu J, Li Y. High-strength and high-ductility nanostructured and amorphous metallic materials. *Adv Mater* 2014, **26**: 5518–5524.

[3] Zhao ST, Zhang RP, Yu Q, *et al.* Cryoforged nanotwinned titanium with ultrahigh strength and ductility. *Science* 2021, **373**: 1363–1368.

[4] Lu K. Making strong nanomaterials ductile with gradients. *Science* 2014, **345**: 1455–1456.

[5] Wu G, Chan KC, Zhu LL, *et al.* Dual-phase nanostructuring as a route to high-strength magnesium alloys. *Nature* 2017, **545**: 80–83.

[6] Liu LL, An XK, Gu XL, *et al.* Nanotwinned CrN ceramics with enhanced plasticity. *Nat Commun* 2025, **16**: 5934.

[7] Zhang Y, Zhang SW, Zhang AF, *et al.* Breaking the trade-off of hardness–ductility in $(Cr_{1-x}Mo_x)_2AlC$ MAX phase coatings via a hierarchical structure. *J Adv Ceram* 2024, **13**: 1748–1758.

[8] Ming KS, Gu C, Su Q, *et al.* Strength and plasticity of amorphous ceramics with self-patterned nano-heterogeneities. *Int J Plasticity* 2020, **134**: 102837.

[9] Dahlqvist M, Barsoum MW, Rosen J. MAX phases–Past, present, and future. *Mater Today* 2024, **72**: 1–24.

[10] Fu L, Xia W. MAX phases as nanolaminate materials: Chemical composition, microstructure, synthesis, properties, and applications. *Adv Eng Mater* 2021, **23**: 2001191.

[11] Barsoum MW, Radovic M. Elastic and mechanical properties of the MAX phases. *Annu Rev Mater Res* 2011, **41**: 195–227.

[12] Torres C, Quispe R, Calderón NZ, *et al.* Development of the phase composition and the properties of Ti_2AlC and Ti_3AlC_2 MAX-phase thin films–A multilayer approach towards high phase purity. *Appl Surf Sci* 2021, **537**: 147864.

[13] Yuan JH, Wang ZY, Ma GS, *et al.* MAX phase forming mechanism of M–Al–C (M = Ti, V, Cr) coatings: *in situ* X-ray diffraction and first-principle calculations. *J Mater Sci Technol* 2023, **143**: 140–152.

[14] Yuan JH, Wang ZY, Ma GS, *et al.* Effect of phase-structure evolution on mechanical properties of Cr_2AlC coating. *Acta Metall Sin* 2023, **59**: 961–968. (in Chinese)

[15] Yuan JH, Zhou SH, Wu HC, *et al.* Ultrahigh strength-ductility of nanocrystalline Cr_2AlC coating under micropillar compression. *Scripta Mater* 2023, **235**: 115594.

[16] Zhou SH, Yuan JH, Wu HC, *et al.* Size-dependent uniform deformation transitions enabling hardness and toughness enhancement of nanocrystalline Cr_2AlC MAX phase. *J Mater Sci Technol* 2025, **232**: 170–180.

[17] Völker B, Stelzer B, Mráz S, *et al.* On the fracture behavior of Cr_2AlC coatings. *Mater Design* 2021, **206**: 109757.

[18] Konovalikhin SV, Guda SA, Kovalev DY. Composition and structure of $(Zr_{0.37}Ti_{0.63})_3AlC_2$ MAX phase crystals prepared by self-propagating high-temperature synthesis. *Inorg Mate* 2018, **54**: 953–956.

[19] Tunca B, Lapauw T, Karakulina OM, *et al.* Synthesis of MAX phases in the Zr–Ti–Al–C system. *Inorg Chem* 2017, **56**: 3489–3498.

[20] Zapata-Solvas E, Hadi MA, Horlait D, *et al.* Synthesis and physical properties of $(Zr_{1-x},Ti_x)_3AlC_2$MAXphases. *J Am Ceram Soc* 2017, **100**: 3393–3401.

[21] Hadi MA, Roknuzzaman M, Chroneos A, *et al.* Elastic and thermodynamic properties of new $(Zr_{3-x}Ti_x)AlC_2$ MAX-phase solid solutions. *Comput Mater Sci* 2017, **137**: 318–326.

[22] Ali MA, Hossain MM, Hossain MA, *et al.* Recently synthesized $(Zr_{1-x}Ti_x)_2AlC$ $(0 \le x \le 1)$ solid solutions: Theoretical study of the effects of M mixing on physical properties. *J Alloys Compd* 2018, **743**: 146–154.

[23] Azina C, Tunca B, Petruhins A, *et al.* Deposition of MAX phase-containing thin films from a $(Ti,Zr)_2AlC$ compound target. *Appl Surf Sci* 2021, **551**: 149370.

[24] Zhang Z, Duan XM, Jia DC, *et al.* On the formation mechanisms and properties of MAX phases: A review. *J Eur Ceram Soc* 2021, **41**: 3851–3878.

[25] Tian ZH, Zhang PG, Sun WW, *et al.* Vegard's law deviating $Ti_2(Sn_xAl_{1-x})C$ solid solution with enhanced properties. *J Adv Ceram* 2023, **12**: 1655–1669.

[26] Wang KH, Li ZC, Zhang Y, *et al.* Solid solution of zirconium on the M-site in Ti_2AlC MAX phase coatings: Synthesis, structure and mechanical properties. *Surf Interfaces* 2024, **51**: 104678.

[27] Zhang MQ, Wang L, Wang ZY, *et al.* Oxygen-driven shell-like microstructure: A pathway to high-performance PVD Cr coatings for metal protection. *npj Mater Degrad* 2025, **9**: 51.

[28] Cui B, Jayaseelan DD, Lee WE. TEM study of the early stages of Ti_2AlC oxidation at 900 °C. *Scripta Mater* 2012, **67**: 830–833.

[29] Luo Q, Jones AH. High-precision determination of residual stress of polycrystalline coatings using optimised XRD-sin$^2\psi$ technique. *Surf Coat Tech* 2010, **205**: 1403–1408.

[30] Jang JI, Pharr GM. Influence of indenter angle on cracking in Si and Ge during nanoindentation. *Acta Mater* 2008, **56**: 4458–4469.

[31] Kese K, Rowcliffe DJ. Nanoindentation method for measuring residual stress in brittle materials. *J Am Ceram Soc* 2003, **86**: 811–816.

[32] Azina C, Bartsch T, Holzapfel DM, *et al.* Yttrium incorporation in Cr_2AlC: On the metastable phase formation and decomposition of $(Cr,Y)_2AlC$ MAX phase thin films. *J Am Ceram Soc* 2023, **106**: 2652–2665.

[33] Karimi Aghda S, Holzapfel DM, Music D, *et al.* Ion kinetic energy- and ion flux-dependent mechanical properties and thermal stability of (Ti,Al)N thin films. *Acta Mater* 2023, **250**: 118864.

[34] Boyer R, Welsch G, Collings EW. *Materials Properties Handbook: Titanium Alloys*. the Netherlands: ASM International, 1994.

[35] Zhang H, Huang WQ, Lin R, *et al.* Room temperature ferromagnetism in pristine TiO_2 nanoparticles triggered by singly ionized surface oxygen vacancy induced via calcining in different air pressure. *J Alloys Compd* 2021, **860**: 157913.

[36] Ftouni J, Muñoz-Murillo A, Goryachev A, *et al.* ZrO_2 is preferred over TiO_2 as support for the Ru-catalyzed hydrogenation of levulinic acid to γ-valerolactone. *ACS Catal* 2016, **6**: 5462–5472.

[37] Li XJ, Wang SH, Wu GX, *et al.* Oxidation and hot corrosion

behaviors of MAX-phase Ti_3SiC_2, Ti_2AlC, Cr_2AlC. *Ceram Int* 2022, **48**: 26618–26628.
[38] Wang QM, Garkas W, Renteria AF, *et al.* Oxidation behaviour of Ti–Al–C films composed mainly of a Ti_2AlC phase. *Corros Sci* 2011, **53**: 2948–2955.
[39] Zhang AF, Wang KH, Zhang Y, *et al.* Towards developing Ti_2AlC coatings with improved oxidation resistance via Nb solid solution. *J Alloys Compd* 2024, **1002**: 175524.
[40] Ougier M, Michau A, Schuster F, *et al.* Effects of HiPIMS discharges and annealing on Cr–Al–C thin films. *Surf Coat Tech* 2020, **399**: 126141.
[41] Cao L, Zhu XH, Fu S, *et al.* Stabilizing high-entropy MAX phases by incorporating tin. *J Adv Ceram* 2025, **14**: 9221028.
[42] Tunca B, Lapauw T, Delville R, *et al.* Synthesis and characterization of double solid solution $(Zr,Ti)_2(Al,Sn)C$ MAX phase ceramics. *Inorg Chem* 2019, **58**: 6669–6683.
[43] Yang W, Shen JX, Wang ZY, *et al.* Mechanical and electrochemical properties of $(MoNbTaTiZr)_{1-x}N_x$ high-entropy nitride coatings. *J Mater Sci Technol* 2025, **208**: 78–91.
[44] Chen XJ, Du Y, Chung YW. Commentary on using H/E and H^3/E^2 as proxies for fracture toughness of hard coatings. *Thin Solid Films* 2019, **688**: 137265.
[45] Fang XF, Bishara H, Ding K, *et al.* Nanoindentation pop-in in oxides at room temperature: Dislocation activation or crack formation. *J Am Ceram Soc* 2021, **104**: 4728–4741.
[46] Huang H, Jiang MQ, Yan JW. New evidences for understanding the serrated flow and shear band behavior in nanoindentation of metallic glasses. *J Alloys Compd* 2021, **857**: 157587.
[47] Schwiedrzik J, Raghavan R, Bürki A, *et al. In situ* micropillar compression reveals superior strength and ductility but an absence of damage in lamellar bone. *Nat Mater* 2014, **13**: 740–747.
[48] Cook RF, Pharr GM. Direct observation and analysis of indentation cracking in glasses and ceramics. *J Am Ceram Soc* 1990, **73**: 787–817.
[49] Barsoum MW, Zhen T, Kalidindi SR, *et al.* Fully reversible, dislocation-based compressive deformation of Ti_3SiC_2 to 1 GPa. *Nat Mater* 2003, **2**: 107–111.
[50] Tang LT, Zhu DG, Sun Z, *et al.* Microstructure and mechanical properties of Al–Ti–Zr intermetallic compounds prepared by vacuum hot pressing. *Vacuum* 2018, **150**: 166–172.
[51] Zhao JT, Zhang JY, Yuan HZ, *et al.* Alloying effects on ductility of nanostructured Cu–X (X = Zr and W) thin films. *Scripta Mater* 2018, **152**: 146–149.
[52] Maita JM, Rommel S, Davis JR, *et al.* Grain size effect on the mechanical properties of nanocrystalline magnesium aluminate spinel. *Acta Mater* 2023, **251**: 118881.
[53] Mathews NG, Lambai A, Hans M, *et al.* The effect of elastic–plastic mismatch and interface proximity on the fracture toughness of Ti–TiN thin films. *Adv Eng Mater* 2025, **27**: 2500285.
[54] Xu XQ, Wang Y, Guo AR, *et al.* Enhanced plasticity by nanocrystallite in bulk amorphous Al_2O_3–ZrO_2–Y_2O_3. *Int J Plasticity* 2016, **79**: 314–327.
[55] Qian WF, Ning BK, Wang S, *et al.* Hierarchically structured ceramic coatings based on zirconia and magnesium oxide with high toughness. *Adv Funct Mater* 2025, **35**: 2418312.
[56] Hu XX, Liu NH, Jambur V, *et al.* Amorphous shear bands in crystalline materials as drivers of plasticity. *Nat Mater* 2023, **22**: 1071–1077.
[57] Ming KS, Zhu ZW, Zhu WQ, *et al.* Enhancing strength and ductility via crystalline-amorphous nanoarchitectures in TiZr-based alloys. *Sci Adv* 2022, **8**: eabm2884.
[58] Griesbach C, Bronkhorst CA, Thevamaran R. Crystal plasticity simulations reveal cooperative plasticity mechanisms leading to enhanced strength and toughness in gradient nanostructured metals. *Acta Mater* 2024, **270**: 119835.
[59] Yu WB, Vallet M. Atomic level decomposition mechanism of Ti_2AlC into TiC_x. *Scripta Mater* 2023, **236**: 115645.
[60] Cui B, Jayaseelan DD, Lee WE. Microstructural evolution during high-temperature oxidation of Ti_2AlC ceramics. *Acta Mater* 2011, **59**: 4116–4125.
[61] Bai YL, He XD, Wang RG, *et al.* High temperature physical and mechanical properties of large-scale Ti_2AlC bulk synthesized by self-propagating high temperature combustion synthesis with pseudo hot isostatic pressing. *J Eur Ceram Soc* 2013, **33**: 2435–2445.
[62] Bai YL, He XD, Zhu CC, *et al.* Microstructures, electrical, thermal, and mechanical properties of bulk Ti_2AlC synthesized by self-propagating high-temperature combustion synthesis with pseudo hot isostatic pressing. *J Am Ceram Soc* 2012, **95**: 358–364.
[63] Wang XH, Zhou YC. Solid–liquid reaction synthesis and simultaneous densification of polycrystalline Ti_2AlC. *Z Für Met* 2002, **93**: 66–71.
[64] Xie X, Yang R, Cui YY, *et al.* Fabrication of textured Ti_2AlC lamellar composites with improved mechanical properties. *J Mater Sci Technol* 2020, **38**: 86–92.
[65] Ying GB, He XD, Li MW, *et al.* Synthesis and mechanical properties of high-purity Cr_2AlC ceramic. *Mat Sci Eng A-Struct* 2011, **528**: 2635–2640.
[66] Li SB, Yu WB, Zhai HX, *et al.* Mechanical properties of low temperature synthesized dense and fine-grained Cr_2AlC ceramics. *J Eur Ceram Soc* 2011, **31**: 217–224.
[67] Bao YW, Wang XH, Zhang HB, *et al.* Thermal shock behavior of Ti_3AlC_2 from between 200 °C and 1300 °C. *J Eur Ceram Soc* 2005, **25**: 3367–3374.
[68] Wang XH, Zhou YC. Microstructure and properties of Ti_3AlC_2 prepared by the solid–liquid reaction synthesis and simultaneous *in situ* hot pressing process. *Acta Mater* 2002, **50**: 3143–3151.
[69] Hu CF, He LF, Liu MY, *et al. In situ* reaction synthesis and mechanical properties of V_2AlC. *J Am Ceram Soc* 2008, **91**: 4029–4035.
[70] Meng FL, Zhou YC, Wang JY. Strengthening of Ti_2AlC by substituting Ti with V. *Scripta Mater* 2005, **53**: 1369–1372.
[71] He GQ, Zhang Y, Yao P, *et al.* A novel medium-entropy $(TiVNb)_2AlC$ MAX phase: Fabrication, microstructure, and properties. *J Mater Sci Technol* 2023, **137**: 91–99.
[72] Ma K, Shi XG, He GQ, *et al. In situ* reaction synthesis, microstructure and thermomechanical properties of novel medium-entropy $(Ti,V,Nb,Ta)_2AlC$ ceramics. *Ceram Int* 2023, **49**: 21206–21212.
[73] Zhang FY, Yu GX, Yan S, *et al.* Phase formation and microstructure evolution of plasma sprayed Cr_2AlC MAX phase coatings under post annealing. *Ceram Int* 2022, **48**: 26063–26071.